Received: 21 November 2017 | Revised: 3 April 2018 | Accepted: 7 April 2018

DOI: 10.1002/nbm.3937

SPECIAL ISSUE REVIEW ARTICLE

WILEY NMR IN BIOMEDICINE

Cancer in the crosshairs: targeting cancer metabolism with hyperpolarized carbon-13 MRI technology

Cornelius von Morze[1] | Matthew E. Merritt[2]

[1]Department of Radiology and Biomedical Imaging, University of California, San Francisco, CA, USA

[2]Department of Biochemistry and Molecular Biology, University of Florida, Gainesville, FL, USA

Correspondence
Matthew E. Merritt, Department of Biochemistry and Molecular Biology, University of Florida, Gainesville, FL 32610, USA.
Email: matthewmerritt@ufl.edu

Funding information
Division of Materials Research, Grant/Award Number: DMR1644779; Eunice Kennedy Shriver National Institute of Child Health and Human Development, Grant/Award Number: R01HD087306; National Institute of Biomedical Imaging and Bioengineering, Grant/Award Number: P41EB013598; National Institute of Diabetes and Digestive and Kidney Diseases, Grant/Award Numbers: K01DK099451, R01DK105346, R01DK112685 and U24DK097209; National Institute of General Medical Sciences, Grant/Award Number: P41GM122698

Magnetic resonance (MR)-based hyperpolarized (HP) ^{13}C metabolic imaging is under active pursuit as a new clinical diagnostic method for cancer detection, grading, and monitoring of therapeutic response. Following the tremendous success of metabolic imaging by positron emission tomography, which already plays major roles in clinical oncology, the added value of HP ^{13}C MRI is emerging. Aberrant glycolysis and central carbon metabolism is a hallmark of many forms of cancer. The chemical transformations associated with these pathways produce metabolites ranging in general from three to six carbons, and are dependent on the redox state and energy charge of the tissue. The significant changes in chemistry associated with flux through these pathways imply that HP imaging can take advantage of the underlying chemical shift information encoded into an MR experiment to produce images of the injected substrate as well as its metabolites. However, imaging of HP metabolites poses unique constraints on pulse sequence design related to detection of X-nuclei, decay of the HP magnetization due to T_1, and the consumption of HP signal by the inspection pulses. Advancements in the field continue to depend critically on customization of MRI systems and pulse sequences for optimized detection of HP ^{13}C signals, focused largely on extracting the maximum amount of information during the short lifetime of the HP magnetization. From a clinical perspective, the success of HP ^{13}C MRI of cancer will largely depend upon the utility of HP pyruvate for the detection of lactate pools associated with the Warburg effect, though several other agents are also under investigation, with novel agents continually being formulated. In this review, the salient aspects of HP ^{13}C imaging will be highlighted, with an emphasis on both technological challenges and the biochemical aspects of HP experimental design.

KEYWORDS

dynamic nuclear polarization, lactate, metabolism, pyruvate, radiology, Warburg effect

1 | INTRODUCTION

Hyperpolarized (HP) MRI using ^{13}C-enriched substrates is rapidly developing as a human diagnostic modality, with multiple National Institutes of Health grants already underwriting a variety of clinical trials. The technical challenges associated with HP imaging are considerable, but the unique metabolic information naturally encoded into the experiment promises to transform medical imaging. While positron emission tomography (PET) will always remain more sensitive than ^{13}C MRI, the lack of chemical specificity associated with PET makes label uptake and deposition the primary observable. Metabolic turnover information in PET is only accessible indirectly by secondary modeling of the label distribution. In contrast, HP ^{13}C MRI uniquely measures both label uptake *and* its subsequent reaction to form metabolic products. The primary objective of the HP-MRI

community is the demonstration that such direct metabolic information provides "actionable intelligence" regarding clinically important pathophysiologies, especially cancer.

While dynamic nuclear polarization (DNP) had been theorized[1] and successfully demonstrated[2] in the 1950s, it was the realization by Ardenkjaer-Larsen et al. of a fast dissolution technique (d-DNP) that enabled the production of hyperpolarized contrast agents with ^{13}C polarizations in excess of 20%, as opposed to the parts-per-million polarization available at thermal equilibrium.[3] Previous reviews have given a more complete description of the phenomena of DNP and appropriate hardware design for sample production.[4] In brief, the metabolic substrate of interest is mixed with a free radical or electronic paramagnetic agent (EPA), which provides the source of electrons necessary for the DNP mechanism to function. The sample is frozen in a high magnetic field at temperatures close to 1 K, and subsequently irradiated with a microwave frequency close to the electron spin resonance frequency. After a suitable time for the transfer of spin order from the electrons to the dipolar coupled nuclei, the sample is rapidly melted with a bolus of superheated water, providing the HP contrast agent. For human studies, each sample is subject to rigorous quality control to confirm suitability for human use including criteria for sterility, EPA filtration, pH, temperature, etc.[5]

HP [1–^{13}C]pyruvate[6] has been the most widely used imaging agent since the inception of d-DNP.[3] A confluence of several considerations make [1–^{13}C]pyruvate an excellent metabolic imaging agent. From a physical perspective, neat pyruvic acid readily solubilizes the trityl radical, the most common source of free electrons for hyperpolarized targets. Additionally, neat pyruvic acid is 14.4 M in concentration, meaning that a concentrated solution of HP pyruvate can be generated from a relatively small sample of pyruvic acid. The high concentration of ^{13}C spins in the pyruvic acid target results in a short buildup time constant, reducing the time required to polarize each sample.[7] The C1 position of pyruvate is distal from the methyl protons, and hence the T_1 of the carbon in solution is long, approximately 55 s in the presence of radical, and 25 s *in vivo* at 3 T.[8] The lifetime of the HP ^{13}C label depends on the exponential T_1 decay rate of the labeled nucleus, which is proportional to the half-life as commonly specified in PET (i.e. by a factor of ln 2). T_1 thus naturally defines the length of the carbon-13 imaging window. While acquisition of conventional MR spectroscopic imaging (MRSI) data typically requires several minutes, HP ^{13}C MRI data must ideally be acquired in a time that is short relative to T_1. This challenge has spurred the development of specialized rapid HP MRI pulse sequences, which have often been implemented (with an eye on clinical translation) on clinical MRI systems specially customized for ^{13}C MRI acquisition. From a biochemistry perspective, pyruvate occupies a central role in energy metabolism, sitting at the terminal end of glycolysis and at the entry to the tricarboxylic acid (TCA) cycle, where it is oxidized to produce NADH necessary for oxidative phosphorylation. Alternatively, pyruvate can pass through alanine

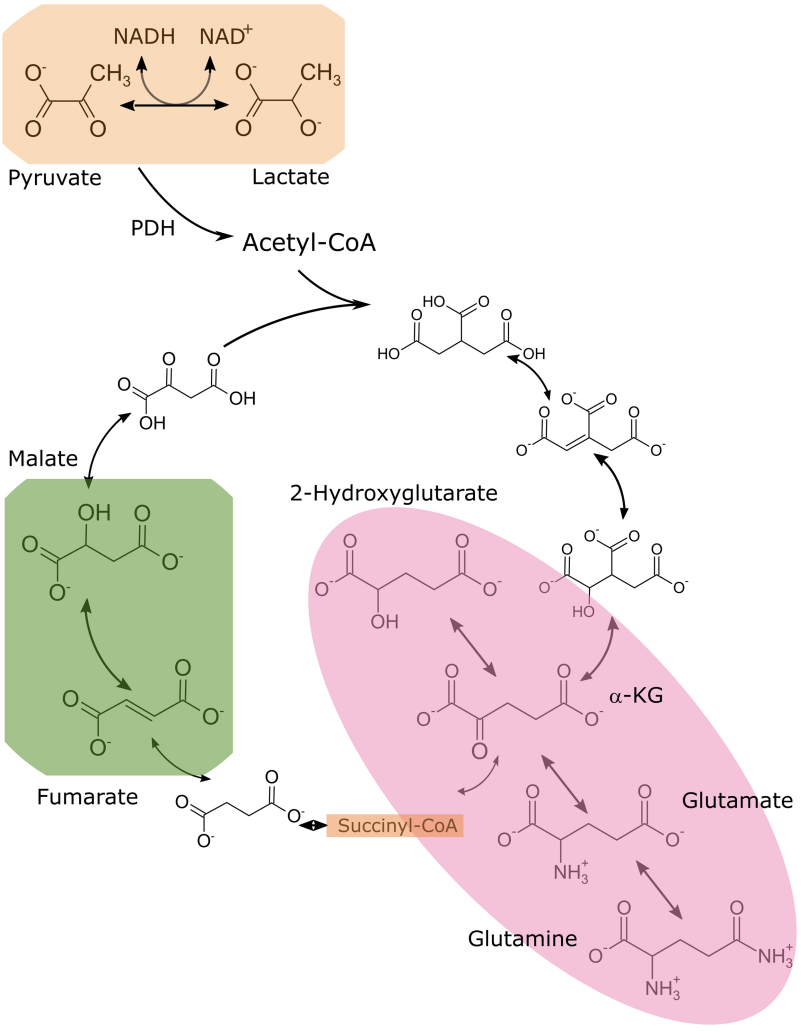

FIGURE 1 Diagram of central metabolism, the primary target of HP-based imaging methods. Glycolytic metabolism (orange), glutamine metabolism (pink), and the detection of tumor necrosis via release of fumarase from the intracellular compartment (green) are current targets for hyperpolarized imaging

aminotransferase (ALT) to form alanine, or through pyruvate carboxylase to produce oxaloacetate (OAA). Perhaps most importantly, pyruvate is in rapid exchange with lactate through the NADH-dependent enzyme lactate dehydrogenase (LDH). Due to overproduction of lactate associated with Warburg metabolism[9] and cancer (Figure 1), pyruvate has found its widest application in cancer detection and grading. It has also found application in monitoring the effects of cancer treatment and its effects on glycolytic metabolism.[10-12]

2 | BIOCHEMICAL ASPECTS OF HP ^{13}C STUDIES OF CANCER METABOLISM

2.1 | Initial insights into cancer metabolism

Initial work by the inventors of the d-DNP method in a rat P22 sarcoma model clearly demonstrated the potential for lactate detection using HP [1–^{13}C]pyruvate.[6] Paired with excellent results acquired using a ^{13}C chemical shift imaging (^{13}C-CSI) pulse sequence, the authors generated a forward-looking discussion that successfully outlined multiple future research paths. First, by localized *in vivo* imaging, it was experimentally determined that the P22 tumor tissue had a significantly larger HP lactate signal, and that inflowing blood was not a significant source of this signal. As tumors initially grow, they are often characterized by increased vascularity; if blood was a primary source of lactate, it would be difficult to deconvolve the effect on apparent lactate conversion in tumor tissues. Furthermore, adjacent healthy tissues produced more alanine and less lactate, suggesting good specificity for HP lactate as a biomarker for cancer detection. Conversely, the authors also considered the possibility that necrosis could be a confounding factor in the interpretation of HP images, and suggested that gadolinium-based perfusion experiments could serve to detect necrosis, i.e. identify non-metabolic areas within the tumor. This idea later found fruit as part of a rigorous approach to model selection and image reconstruction.[13] Efforts are also continuing to integrate perfusion imaging data derived from metabolically inert HP tracers such as [^{13}C]urea with metabolic data from [1–^{13}C]pyruvate.[14]

Seminal preclinical work was produced by Day et al. in EL-4 mouse lymphoma cell culture.[15] Previous experience in the laboratory left them uniquely prepared to interpret the results obtained with HP pyruvate.[16] Using a truncated set of modified Bloch equations,[17] deposition of HP label from [1–^{13}C]pyruvate into the lactate pool was modeled as a function of time, with excellent agreement between the simulations and the data. Due to uncertainties surrounding the delivery of the substrate and the possibility of multiple compartments (intra- versus extracellular), the authors referred to the derived rate constant, *k*, as "apparent". A key component of their experimental design was the addition of increasing amounts of exogenous lactate to the cell culture. Higher concentrations of lactate produced larger HP [1–^{13}C]lactate signals after pyruvate injection. If pyruvate addition to the culture produced a large net flux of pyruvate to lactate, the size of the derived lactate signal would not display a strong dependence on the size of the lactate pool, but would rather be a metric of LDH flux. If a large net flux from pyruvate to lactate were induced, this would also imply net consumption of the NADH cofactor of LDH. Instead, increasing HP lactate signal as a function of exogenous lactate indicated that pyruvate is in a rapid, near-equilibrium exchange with lactate in EL-4 cells. This realization is essential for proper interpretation of HP data, and was subsequently examined and re-affirmed in *in vivo* studies.[18] If a rapidly exchanging pool of a product metabolite is present, the observed data depends as much or more on the relative pool sizes as on enzyme activities. An essential and often recapitulated characteristic of the spectra was the notable increase in lactate signal *in vivo* when localized to the tumor versus the vasculature. Treatment of EL-4 tumor bearing mice with etoposide resulted in cell death within the tumor and a consequent decrease in generated lactate. In cell culture, the mechanism of decreased HP lactate signal production could be elucidated more effectively. Treatment by etoposide caused a loss of the NADH cofactor, while LDH activity was preserved. LDH activity only became significantly lower at later time points. This manuscript therefore outlined two mechanisms controlling HP lactate production from pyruvate; lactate pool size and NADH availability. LDH abundance and activity were not sources of control for the appearance of HP lactate signal.

While conversion of HP [1–^{13}C]pyruvate to lactate has been the focal point of HP ^{13}C cancer imaging research, conversion to alanine is also of great interest in certain tumors. For example, Hu et al. showed that increased conversion of HP [1–^{13}C]pyruvate to alanine precedes tumorigenesis in a switchable, transgenic mouse model of liver cancer.[19]

2.2 | Application of HP [1–^{13}C]pyruvate to prostate cancer

Interest in improving the clinical assessment of prostate cancer has largely driven the development of HP ^{13}C MRI, as proximity to the bladder limits the applicability of nuclear medicine. Prostate cancer is biologically diverse, with disease aggressiveness ranging from indolence to metastatic mortal disease.[20] The primary clinical means of diagnosis is serum testing for prostate-specific antigen (PSA), but the test suffers from low specificity, a non-trivial false negative rate, and overdiagnosis leading to overtreatment of relatively indolent tumors.[21] Standard ^{18}F-FDG PET is not useful for initial staging and has limited ability to diagnose the biochemical failure that precedes recurrence after initial treatment.[22] As such, new methods for detecting and staging prostate cancer, as well as detecting response to therapy, could significantly improve patient care.

A widely used model of human prostate cancer, the transgenic adenocarcinoma of mouse prostate (TRAMP) mouse,[23] was an initial target for preclinical investigation. Albers et al. acquired MRSI data with HP [1–^{13}C]pyruvate in TRAMP mice in comparison with histologic grading.[24] Significantly, HP lactate levels correlated strongly with histologic grade. To facilitate analysis of HP pyruvate metabolism, the authors normalized metabolite signals by "total hyperpolarized carbon", or a sum of all HP metabolites over all space. This approach could also be extended across dynamic time points to produce normalized kinetic curves that, in analogy to PET methods, express the intensity at any point as a fraction of

the total carbon signal. This approach has proven to be robust, and subsequently was shown to produce estimates of kinetic rates that are essentially equivalent to first order rate constant models.[25]

Further insights into the kinetics of HP pyruvate metabolism were developed using both rats and the TRAMP model.[26] While the *in vivo* condition obviously does not support the assumptions inherent in Michaelis–Menten (MM) kinetics, an MM type model was used to assess the dose–response relationship between pyruvate delivery and lactate appearance. Appearance of HP lactate and alanine as a function of injected pyruvate mass was used to extract apparent V_{max} and k_m MM kinetic parameters. Initial reaction rates, V_0, for lactate production were higher in the TRAMP model, and were lowered following bicalutamide treatment. A similar theoretical treatment was used in breast cancer cell culture by Harris et al., where it was found that flux through moncarboxylate transporter 1 (MCT-1), the enzyme that transports pyruvate into the cell, governed the appearance of lactate more strongly than LDH activity.[27] Increased lactate efflux via upregulation of MCT-4 has also been shown to contribute substantially to the increased HP lactate signal observed in cancer.[28]

With the plethora of preclinical results establishing a sound rationale for human imaging, a safety study for pyruvate tolerance in humans was the obvious and necessary step for further development of HP imaging as a clinical technique. The first publication detailing the human use of HP pyruvate as an imaging substrate established 235mM as a safe concentration for injection, without assaying more concentrated solutions.[29] It was also anecdotally shown that HP pyruvate could diagnose prostate cancer in cases where it was not previously detected. Subsequently, HP pyruvate was also used in humans to monitor myocardial metabolism.[30]

The alternative imaging substrate [2-^{13}C]pyruvate has found application in systems exhibiting robust oxidative flux,[31-33] but has not found extensive application in cancer imaging to date.[34]

2.3 | HP ^{13}C studies of glutamine metabolism

Another common perturbation of intermediary metabolism in tumors is increased glutamine consumption (Figure 1). Glutamine is in ready exchange with TCA cycle intermediates via glutaminase and glutamate dehydrogenase, and has multiple effects on tumor bioenergetics and whole body metabolism in the presence of cancer.[35] Glutamine is a nutrient that can directly provide energy in the absence of glucose via glutaminolysis, provides carbon skeletons for macromolecule synthesis, and can dampen the effects of oxidative stress inside the tumor. It is also in the pathway associated with the oncometabolite 2-hydroxyglutarate (2HG), which can be detected in some instances by ^{1}H spectroscopy.[36] The essential role of glutamine in cancer metabolism makes it a natural target for imaging, much like lactate. Moreover, high dose glutamine treatment was recently FDA approved for treating acute complications of sickle cell disease,[37] evidencing a strong safety profile. Unlike HP pyruvate, however, the optimal choice of glutamine isotopomer is less clear. Both the C1 and C5 positions of glutamine have only α-protons as a primary source of relaxation, and hence their T_1 values are relatively long in solution (>15 s), but show a strong field dependence associated with the chemical shift anisotropy of the carbonyls.[38,39] However, the relatively small changes in chemical shift upon metabolic transformation to glutamate make ready measurement of reaction kinetics more problematic.

Initial studies used [5-^{13}C]glutamine in HEP-G2 cancer cell suspension to measure [5-^{13}C]glutamate production following flux through glutaminase.[40] The chemical shift between the two C5-labeled molecules was about 3.4 ppm, which is easily resolved in cell culture at high field, but is a relatively small difference to measure at clinical field strengths. The authors speculated that, due to the central role of glutamine in biosynthesis, perhaps HP imaging could detect more rapidly proliferating cell types. Subsequent work improved the preparation of glutamine for the hyperpolarization process and showed a treatment response in cell culture.[41] The difference in chemical shift between C1-labeled glutamate and glutamine is even smaller, but rapid exchange between [1–^{13}C]glutamine and [1–^{13}C]2HG can still be monitored with HP imaging.[39] This paper demonstrates a primary strength of HP-based imaging kinetics. While a battery of ^{13}C isotopomer results were used to confirm and justify the imaging observations, the direct observation of flux from the precursor to the product is the most powerful proof possible of the metabolic relationship. Carbon-13 isotopomer analysis showed that in the patient-derived chondrosarcoma cells glutamine had multiple competing fates, including oxidation, reductive carboxylation, and 2HG production via the mutated isocitrate dehydrogenase (IDH) enzyme. In contradistinction, [U-^{13}C]glucose did not readily label the 2HG pool, implying compartmentation of 5-carbon metabolism that is distinct to the cancer cell. In this way, HP glutamine imaging has directly identified a metabolic target for therapy. A similar hypothesis was previously studied using HP [1–^{13}C]α-KG.[42] In that case, the product [1–^{13}C]2HG was observed and assayed as diagnostic of IDH1 mutation. However, the transport of α-KG to the intracellular space is not through a readily defined transporter such as MCT-I. It is possible that these results were directly related to necrosis in the tumors that were imaged.

2.4 | HP ^{13}C imaging of tumor necrosis

Tumor necrosis and apoptosis is common due to failed angiogenesis in the tumor as it gains in physical size. This concomitant physical phenomenon associated with cancer progression is the basis for HP fumarate imaging.[43] Fumarate is a 4-carbon intermediate of the TCA cycle that, much like α-KG, contains two carboxyl moieties that restrict its ready penetration of the cellular membrane. When labeled at the C1 and C4 positions (Figure 1), flux through fumarase produces [1,4-$^{13}C_2$]malate, which is sufficiently resolved spectrally from the fumarate precursor to allow identification of both labeled sites.[43] In EL-4 cell culture, malate production was barely measurable in healthy cells, but apoptosis following etoposide treatment resulted in increased malate signal strength. Subsequent lysis of the cells increased the malate response further.

Gallagher et al. proposed that the induction of necrosis could be correlated with treatment response, and hence HP fumarate imaging could be used to calibrate appropriate dosing for chemotherapeutics. A similar result was subsequently obtained in the detection of renal acute tubular necrosis.[44] Note that HP fumarate imaging does not detect TCA cycle metabolism, but rather the liberation of fumarate from the intracellular compartment.

2.5 | HP ^{13}C pH imaging

Another common feature of cancer is acidification of the extracellular space,[45] which has been associated with metastatic potential. As such, pH imaging could be valuable for identifying the most dangerous tumors. The genre of pH imaging is far too extensive to review in even the most cursory fashion in this context, but several HP probes have been proposed. HP ^{13}C-bicarbonate imaging is inherently attractive, as bicarbonate is the primary buffer in the bloodstream. As such, there should be no limitation on the use of a bicarbonate based imaging agent. Unfortunately, the T_1 (<10 s) of the exchanging bicarbonate and CO_2 limits its effectiveness.[46] Related work based on pH-responsive chemical shifts in HP Good's buffers,[47] zymonic acid,[48] and ^{15}N-based agents,[49] as well as other probes, has been reported.

3 | CUSTOMIZATION OF MRI SCANNER HARDWARE FOR HP ^{13}C STUDIES

3.1 | Basic requirements and fundamental considerations

While ^{13}C is of course frequently utilized in preclinical MR systems, development of ^{13}C methods in clinical systems was limited prior to hyperpolarization, due to the intrinsically low sensitivity of ^{13}C. In addition to initial HP ^{13}C studies on preclinical systems, a great deal of HP ^{13}C MRI development has been conducted on clinical scanners in recent years, with initial testing in small animals allowing rapid clinical translation of HP [1–^{13}C]pyruvate. Beyond standard MRI system features needed for ^{1}H imaging, the excitation and detection of HP ^{13}C signals require supplementary RF coils and amplifiers designed to operate at ^{13}C frequencies. In clinical systems, ^{1}H excitation is usually provided by a large body coil, which provides a highly uniform transmit pattern albeit with high power requirements, while signal reception is by an array of smaller coil elements with much higher sensitivity of detection and added capability for parallel imaging.[50-52] To date, the excitation field for HP ^{13}C MRI studies has typically been provided by a variety of insert coil designs, of volume or surface coil type, although commercial development of a ^{13}C-tuned body coil for a human scanner is underway. A "clamshell" insert volume transmitter design, producing a reasonably uniform transmit pattern, has been applied for the initial human studies at multiple sites.[29,30] HP ^{13}C signal reception has been by surface coils (individual or phased array) or small volume transceiver coils, which have more uniform reception fields at the expense of lower sensitivity.

Since HP magnetization is pre-polarized, the SNR of HP ^{13}C MRI detection is approximately independent of readout field strength, although signal increases linearly with precession frequency in accordance with Faraday's law, with body noise also increasing approximately linearly.[53] Readout at sufficiently high frequency is therefore desirable to help reach body noise dominance and to obtain wide spectral separation of individual resonances, although relaxation times of important carbonyl carbons also decline with increasing field strength.[38] Fortunately, a good trade-off is achieved at clinical field strengths of 1.5-3 T, which crucially also provide high quality conventional ^{1}H imaging. However, depending on coil size, ^{13}C coil noise can contribute significantly to total noise even at 3 T,[53] suggesting a potential future role for cryogenic cooling of HP ^{13}C MRI detection coils for optimal SNR.

3.2 | ^{13}C phased array RF reception

Signal reception via phased array RF coils is the standard of care for conventional ^{1}H MRI, and is likely to be similarly crucial for HP ^{13}C MRI. Phased arrays were originally conceived to provide higher sensitivity of detection for ^{1}H MRI over the same volume as a single larger coil, albeit with loss of spatial uniformity.[51] More recently, they were also found to enable accelerated imaging via parallel imaging.[50,52] Similarly, phased array ^{13}C coils have also shown the potential to significantly enhance the sensitivity and/or coverage of HP ^{13}C MRI,[54] and when paired with paired with appropriate parallel imaging acquisition and reconstruction methods significantly accelerate HP ^{13}C imaging acquisition.[55-58] Separation of transmit and receive coils requires some RF system customizations. For initial work, ^{13}C receive coils were actively detuned during transmission via PIN diodes in order to avoid blocking the ^{13}C transmit field and to protect ^{13}C receiver electronics.[55,58] Further work added active detuning of the transmit coil during signal reception in order to avoid coupling of signal and/or noise into the receive coils.[56] Despite being tuned to different frequencies, ^{13}C coils have been equipped with passive ^{1}H blocking, and vice versa, to prevent residual crosstalk. ^{13}C RF coil design extends to the connected signal preamplifiers (based on low noise GaAs FETs), which have been mounted on or near the coils, and in the case of phased arrays have been noise matched but impedance mismatched to the coil,[55,58] to help minimize inductive coupling between elements.[51] Crucially, preamplifiers must maintain stability over varying source impedances seen inside the MRI scanner. Photographs of a clinical 3 T MRI scanner configured for a HP ^{13}C MRI scan, with insert volume coil ^{13}C transmission and phased array ^{13}C reception, are shown in Figure 2.

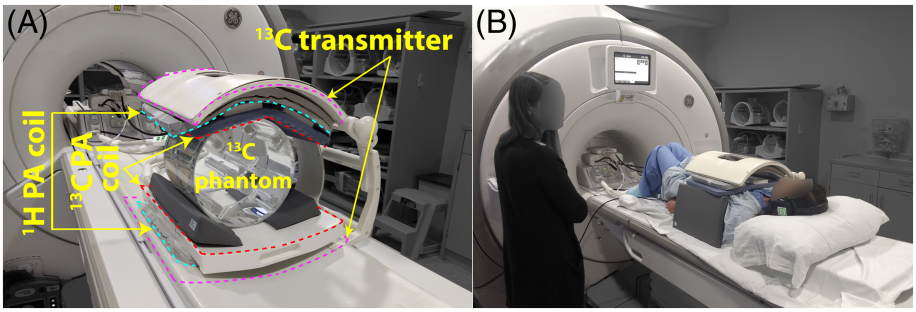

FIGURE 2 Configuration of clinical 3 T MRI scanner hardware for abdominal HP ^{13}C MRI scanning, set up for both phantom testing (A) and human studies (B). The ^{13}C phased array (PA) receiver coil (Rapid Biomedical, Rimpar, Germany) is placed inside the clamshell insert ^{13}C transmitter. A ^{1}H phased array receiver coil is also included to ensure high quality anatomic ^{1}H imaging

3.3 | Insert gradients

A purely hardware-based method for accelerating the acquisition of HP ^{13}C MRI data is the use of insert gradient coils,[59] which can provide much higher peak amplitudes and slew rates due to their smaller size, potentially addressing the greater gradient area demands for ^{13}C MRI due to its four times lower gyromagnetic ratio. Insert gradient systems are however practically challenging due to their large size and weight, as well as potentially significant heating and Lorentz forces experienced during imaging.

3.4 | Indirect detection

Configuration of MRI systems for dual ^{13}C/^{1}H RF stimulation may be beneficial for HP ^{13}C MRI studies. Application of ^{1}H decoupling has been shown to modestly improve the detection of HP [1–^{13}C]lactate generated from [1–^{13}C]pyruvate, by eliminating *J* coupling to the distant methyl protons.[60,61] A new, potentially attractive alternative approach to *in vivo* HP ^{13}C detection is ^{1}H detection following polarization transfer via *J* coupling.[62,63] A recent report describes successful implementation of spectrally selective polarization transfer to the methyl protons in HP [1–^{13}C]lactate generated *in vivo* from HP [1–^{13}C]pyruvate, using a reverse INEPT pulse sequence[64] implemented on a preclinical MRI scanner.[63] This approach has significant theoretical advantages including increased sensitivity of detection and reduced gradient requirements to attain a given spatial resolution, due to the higher gyromagnetic ratio of ^{1}H. It could also greatly simplify the acquisition of HP ^{13}C data by eliminating the need for specialized ^{13}C receiver coils and electronics. In this case, the MRI system must be configured to support simultaneous (or near-simultaneous) pulsing on both ^{13}C and ^{1}H channels. Major challenges for this type of approach include suppression of endogenous ^{1}H signals and minimization of polarization losses over the required evolution times.

4 | HP ^{13}C MRI ACQUISITION PULSE SEQUENCES AND RECONSTRUCTIONS

4.1 | Chemical shift imaging

In terms of special acquisition considerations for HP ^{13}C MRI, the definitive feature of HP magnetization is the omission, as negligible, of T_1 recovery from the Bloch equation. HP ^{13}C magnetization is quickly lost to T_1 and, following RF excitation, T_2 decay. Considering this transient nature of HP magnetization, development of pulse sequence methodology for HP ^{13}C MRI applications has focused on rapidly extracting maximal spatial and spectral information from the short-lived HP signal. While CSI provided a "tried and true" methodology for initial proof of concept studies,[6,65] this approach is extremely limited in terms of spatiotemporal resolution. Moreover, during the slow course of CSI acquisition, HP ^{13}C magnetization is subject to substantial flow and metabolic conversion, as well as T_1 and T_2 decay, all of which can significantly blur the resultant spectroscopic images. Although T_2 decay due to prior pulses in CSI and other phase-encoded approaches can be effectively compensated by employing an increasing flip angle schedule,[66] these fundamental limitations of CSI have led to the development of other more optimal approaches for HP ^{13}C MRI.

4.2 | Fast MRSI approaches

Motivated by the demand for increasing matrix sizes needed to capture high spatial resolution data as well as temporal dynamics, fast MRSI approaches were developed based on superimposing readout gradients onto CSI to accelerate *k*-space coverage, in particular applying echo-planar spectroscopic imaging (EPSI).[67] Initially, flyback EPSI trajectories were used,[67,68] which do not require even-odd echo calibration, but later symmetric trajectories were also used for higher SNR efficiency.[69] To provide further acceleration, several *k*-space undersampling strategies have been developed for HP ^{13}C MRSI, relying on separate assumptions about the source data in order to reconstruct the missing data. These strategies include parallel imaging,[50,52] partial Fourier acquisition,[57,70] and compressed sensing.[71,72] For HP ^{13}C MRSI, strategies based on compressed sensing can be applied especially heavily along the spectral and/or time series dimensions to greatly accelerate the acquisition of spectroscopic

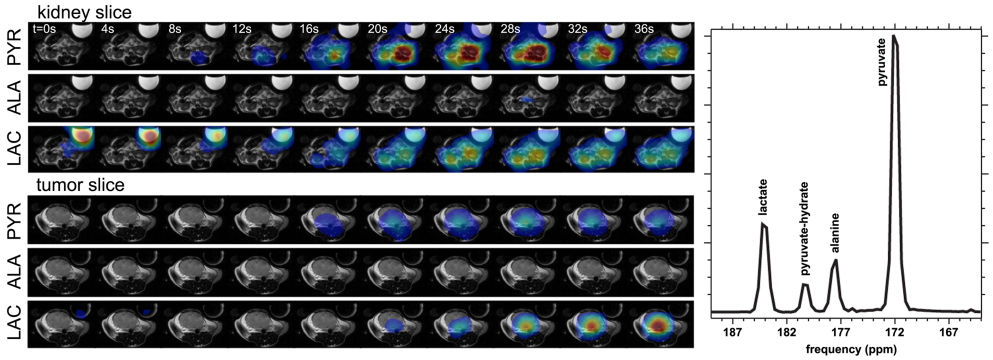

FIGURE 3 Accelerated 3D dynamic HP [1–^{13}C]pyruvate MRSI data series in a transgenic mouse prostate tumor. MRSI data acquisition was accelerated using EPSI as well as data undersampling along the spectral and time series dimensions via compressed sensing. To enhance the dynamic detection of metabolic products, the acquisition also utilized multi-band RF excitation with smaller flip angle on the initial [1–^{13}C] pyruvate (PYR) substrate as compared with metabolic products formed *in vivo*, [1–^{13}C]lactate (LAC) and [1–^{13}C]alanine (ALA). Note that the spectrum on the right is collected from a separate experiment from the images. Left: for comparison, dynamic data from a tumor slice is shown below dynamic data from a kidney slice. Images provided courtesy of Peder EZ Larson, PhD (UCSF)

imaging data,[73] especially for dynamic time series data.[74] Simultaneous with these EPSI-based developments, analogous fast MRSI methods were also developed based on spiral CSI readouts.[75,76] Aside from acceleration, a significant further development was the design of multi-band RF excitation pulses with independent flip angle control over individual metabolites.[77] By applying a smaller flip angle to the initial HP substrate, this approach provides enhanced detection of downstream HP metabolic products formed *in vivo* while minimally perturbing the initial substrate, potentially extending the dynamic imaging window. Dynamic spectroscopic images of a transgenic mouse prostate tumor (TRAMP model),[74] acquired using EPSI acquisition with multi-band excitation and acceleration via compressed sensing, are shown in Figure 3. As an alternative to fully encoded spectroscopy, multi-echo separation of multiple HP ^{13}C resonances is also possible by applying prior knowledge of chemical shifts,[78,79] but care must be taken to ensure good conditioning of the reconstruction problem and account for B_0 inhomogeneity.

4.3 | Imaging approaches

Despite the massive degree of acceleration achievable using these sophisticated MRSI techniques, multiple groups have recently converged on the more straightforward approach of spectral-spatial excitation of individual metabolites followed by rapid spatial encoding (e.g. via echo-planar or spiral readout), with these excitations dynamically interleaved on a metabolite-by-metabolite basis.[80-82] In fact, echo-planar or spiral readout of the individual metabolites is certainly the fastest imaging strategy for the case of a relatively small number of resonances. Moreover, this approach is readily compatible with the idea of independent flip angles on individual metabolites[77] to preserve the magnetization of the source substrate in dynamic studies, and furthermore is more easily integrated with standard clinical imaging frameworks[80] as compared with MRSI. Although water-only spectral-spatial ^{1}H excitation had previously been applied widely to avoid lipid artifact in ^{1}H imaging applications,[83,84] application of this approach for HP ^{13}C MRI was first shown for specifically imaging lactate formed from HP [1–^{13}C]pyruvate *in vivo*,[85] and later extended to interleaved imaging of multiple metabolites.[81] A generic pulse sequence diagram for metabolite-specific imaging of HP ^{13}C metabolites is shown in Figure 4, and mouse tumor images acquired using this approach[80] are shown in Figure 5. Pulse shapes can be individually optimized for each metabolite, or a single shape suitable for all resonances can be designed. Remaining questions around this approach include whether 2D multi-slice or 3D acquisition is optimal for volumetric coverage. 2D acquisition, especially in single shot form, has the benefit of freezing motion effects for each slice. 3D acquisition on the other hand is more amenable to data undersampling strategies, and minimizes potentially significant slice profile effects.[86] Potential drawbacks of the spectral-spatial approach as compared with MRSI include: (i) moderate sensitivity to center frequency

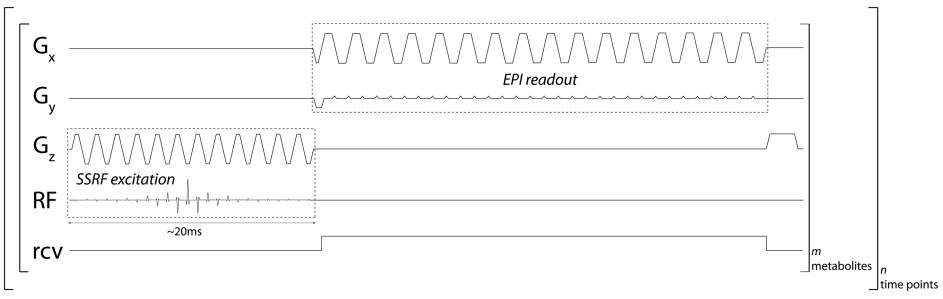

FIGURE 4 Pulse sequence diagram for metabolite-specific imaging method for HP ^{13}C MRI. In this approach, spectral-spatial radiofrequency (SSRF) excitation (left dotted box) is paired with 2D echo-planar imaging readout (right dotted box). The imaging sequence is repeated for multiple metabolites and time points over the course of dynamic imaging data acquisition

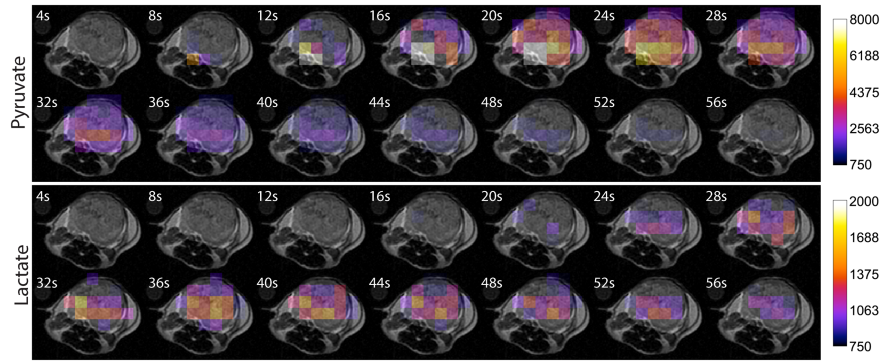

FIGURE 5 Axial dynamic 2D images of HP [1–^{13}C]pyruvate and *in vivo* metabolic product [1–^{13}C]lactate, formed using interleaved metabolite-specific EPI acquisition, in a TRAMP mouse prostate tumor. Metabolites were sequentially excited with a single band spectral-spatial RF pulse and encoded with a single shot symmetric echo planar readout. Data were acquired with a 2 s temporal resolution using an RF-compensated variable flip angle schedule, with an in-plane resolution of 3.3 × 3.3 mm^2 and 10 mm slice thickness. For clarity, every other time frame is shown. To display the images with the same contrast settings, pyruvate was scaled down by a factor of 4. Images provided courtesy of Jeremy W Gordon, PhD (UCSF)

offsets in terms of spatial artifacts and potentially incorrect flip angles, meaning that the center frequency must be set carefully; (ii) some loss of signal due to T_2* decay during the relatively long RF excitation pulses required for spectrally selective excitation; and (iii) introduction of T_2* image blurring during the long readout. Overall, although there are variations on this approach, its familiarity and practicality have led to increasingly wider adoption.

4.4 | Parallel imaging

Parallel imaging[50,52] exploits the spatially varying spatial sensitivities of the individual elements of a phased array coil to perform some of spatial encoding normally performed exclusively by gradient encoding, and is very widely utilized for clinical MRI studies. Initial studies showed the potential for accelerating ^{13}C MRSI by a reduction factor of 2 (i.e. R = 2) using three- and four-element ^{13}C arrays, using SENSE reconstructions.[55,58] However, a particular challenge for HP ^{13}C parallel imaging is the acquisition of coil sensitivity calibration data needed for image reconstruction, since the thermal ^{13}C signal is insufficient for this purpose. An initial study showed the feasibility of autocalibrated spectroscopic HP ^{13}C parallel imaging with outer reduction factor (ORF) up to 3.[57] However, acquiring embedded calibration data during the actual imaging sequence (auto-calibration) limits the achievable acceleration at the generally limited matrix sizes of HP ^{13}C acquisitions. Therefore, a "calibration-less" approach for parallel imaging has been developed, based on randomly undersampling the center of k-space.[56,87] Alternatively, coil sensitivity data can be analytically calculated based on known coil positions, which is valid since the quasi-static electromagnetic regime generally holds at ^{13}C frequencies; this approach has been used to correct ^{13}C images.[88] Ultimately, the degree of acceleration possible via parallel imaging will likely be limited by SNR penalties associated with scan time reduction and/or reconstruction-related losses, known as the g-factor penalty in SENSE reconstruction,[50] which are dependent on both the acceleration scheme and coil geometry.

4.5 | Refocused approaches

While most of the HP ^{13}C pulse sequence methodology developed so far has employed spoiled data acquisition, HP ^{13}C MRI is more limited by T_2* than T_2.[89] Therefore, application of refocused acquisition schemes can offer enhanced sensitivity for detection of HP ^{13}C resonances. Initial studies on imaging single HP ^{13}C resonances utilized balanced SSFP (bSSFP) acquisition for angiography and perfusion imaging.[90-92] Recent work has shown that rat kidneys can be imaged at resolutions approaching 1 mm isotropic using HP ^{13}C probes with bSSFP acquisition.[93,94] Dynamic HP ^{13}C bSSFP images of a transgenic mouse liver tumor are shown in Figure 6, showing the feasibility of HP perfusion imaging to evaluate tumor blood flow. Although extending these results to studies including multiple resonances is challenging due to the complex frequency response of magnetization to SSFP pulse trains,[95,96] an initial study showed that it is possible to model multi-echo bSSFP data in an IDEAL framework and solve for individual metabolites.[78] Moreover, recent work has shown the feasibility of an interleaved frequency-specific bSSFP approach enabled through design of minimum length RF pulses and carefully chosen T_R values.[97]

4.6 | Overall technical outlook and challenges

Collection of HP ^{13}C MRI data depends critically on specialized ^{13}C RF hardware and acquisition pulse sequences. Quantification of HP kinetics remains remarkably challenging, as a full model of substrate delivery, extravasation, and subsequent enzyme-catalyzed metabolism is theoretically justified if not always experimentally necessary.[13] Modeling of the kinetics will always remain dependent on the acquisition scheme due to T_1 relaxation and excitation-mediated depolarization of the HP imaging agent.

On the hardware side, the best solution appears to match the clinical ^{1}H imaging paradigm—excitation by a large, uniform volume coil, followed by phased array surface coil reception for highest sensitivity of detection. A significant remaining challenge is optimizing the receiver coil

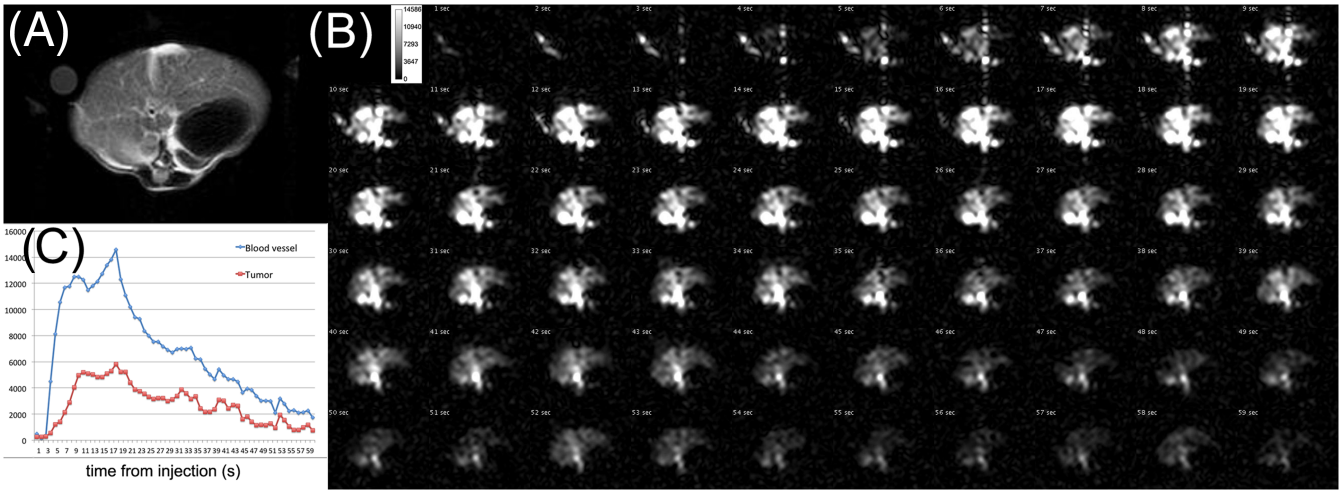

FIGURE 6 Axial dynamic 2D HP ^{13}C bSSFP images (B) of the perfusion agent HP001 (HP bis-1,1-(hydroxymethyl)-[1–^{13}C]cyclopropane-d_8) injected in a transgenic mouse with liver tumor, collected over 1 min (spatial resolution = 2 × 2 mm^2, temporal resolution = 1 s). An axial ^{1}H image of the same slice is also shown (A), as well as dynamic signal plots (C) for an input vessel and tumor region

configuration for each application. On the pulse sequence side, investigators have converged on a handful of successful imaging strategies based largely on spectroscopic imaging or interleaved metabolite-specific imaging. The challenge here is clarifying how to use advanced imaging strategies to maximize the spatiotemporal resolution and coverage of imaging (e.g. parallel imaging and/or compressed sensing), or even the sensitivity of detection (e.g. refocused approaches, indirect detection).

Cost remains a concern for developing a clinical paradigm using hyperpolarized imaging. Almost 2 g of sterile, pyrogen free, [1–^{13}C]pyruvate is needed for a single human examination. When the cost of the free radical in included in the sample preparation, each sample alone can cost as much as 1000 USD. Furthermore, the GE SpinLab clinical polarizer produces a sample suitable for human injection, but a pharmacist is still required to certify that the sample is safe prior to injection. The overhead associated with extra technical staff would be added to the cost of an examination; therefore, a central goal for polarizer development would be a system that removes the need for any monitoring of the imaging agent by humans. While these hurdles are considerable, we expect them to be overcome as higher usage of the methodology drives further improvement to the sample production pipeline.

5 | CONCLUSION

HP ^{13}C imaging continues to evolve rapidly, with research into the basic science as well as imaging methodologies proceeding in a parallel fashion. The chemical selectivity of magnetic resonance has always suggested that it might serve as a powerful metabolic imaging modality, but the advent of HP methods is driving possible clinical applications in new ways. It is likely that multiple different protocols for HP imaging will ultimately be used in practice, depending upon the target organ and pathophysiology. Ongoing clinical trials should establish the efficacy of HP imaging for cancer detection, grading, and treatment response in the near future.

ACKNOWLEDGEMENTS

CVM acknowledges the support of NIH grants K01DK099451 (NIDDK) and P41EB013598 (NIBIB). MM acknowledges the support of NIH-R01DK105346 (NIDDK), R01HD087306 (NICHD), R01DK112685 (NIDDK), P41GM122698 (NIGMS), and U24DK097209 (NIDDK), as well as NSF-DMR1644779 (Division of Material Research).

ORCID

Cornelius von Morze http://orcid.org/0000-0002-3992-1793
Matthew E. Merritt http://orcid.org/0000-0003-4617-9651

REFERENCES

1. Overhauser AW. Polarization of nuclei in metals. *Phys Rev*. 1953;92(2):411.
2. Carver TR, Slichter CP. Polarization of nuclear spins in metals. *Phys Rev*. 1953;92(1):212.
3. Ardenkjaer-Larsen JH, Fridlund B, Gram A, et al. Increase in signal-to-noise ratio of > 10,000 times in liquid-state NMR. *Proc Natl Acad Sci U S A*. 2003;100(18):10158-10163.

4. Comment A, Merritt ME. Hyperpolarized magnetic resonance as a sensitive detector of metabolic function. *Biochemistry*. 2014;53(47):7333-7357.
5. Ardenkjaer-Larsen JH, Leach AM, Clarke N, Urbahn J, Anderson D, Skloss TW. Dynamic nuclear polarization polarizer for sterile use intent. *NMR Biomed*. 2011;24(8):927-932.
6. Golman K, in 't Zandt R, Thaning M. Real-time metabolic imaging. *Proc Natl Acad Sci U S A*. 2006;103(30):11270-11275.
7. Lloyd L, Zoltan K, Craig M, Sherry AD, Matthew M. The effect of ^{13}C enrichment in the glassing matrix on dynamic nuclear polarization of [1-^{13}C]pyruvate. *Phys Med Biol*. 2011;56(5):N85.
8. Golman K, Petersson JS, Magnusson P, et al. Cardiac metabolism measured noninvasively by hyperpolarized ^{13}C MRI. *Magn Reson Med*. 2008;59(5):1005-1013.
9. Warburg O. On the origin of cancer. *Science*. 1956;123(3191):309-314.
10. Asghar Butt S, Søgaard LV, Ardenkjaer-Larsen JH, et al. Monitoring mammary tumor progression and effect of tamoxifen treatment in MMTV-PymT using MRI and magnetic resonance spectroscopy with hyperpolarized [1-^{13}C] pyruvate. *Magn Reson Med*. 2015;73(1):51-58.
11. Canapè C, Catanzaro G, Terreno E, Karlsson M, Lerche MH, Jensen PR. Probing treatment response of glutaminolytic prostate cancer cells to natural drugs with hyperpolarized [5-^{13}C] glutamine. *Magn Reson Med*. 2015;73(6):2296-2305.
12. Silvers MA, Deja S, Singh N, et al. The NQO1 bioactivatable drug, β-lapachone, alters the redox state of NQO1+ pancreatic cancer cells, causing perturbation in central carbon metabolism. *J Biol Chem*. 2017;292(44):18203-18216.
13. Bankson JA, Walker CM, Ramirez MS, et al. Kinetic modeling and constrained reconstruction of hyperpolarized [1-13C]-pyruvate offers improved metabolic imaging of tumors. *Cancer Res*. 2015;75(22):4708-4717.
14. Chen H-Y, Larson PE, Bok RA, et al. Assessing prostate cancer aggressiveness with hyperpolarized dual-agent 3D dynamic imaging of metabolism and perfusion. *Cancer Res*. 2017;77(12):3207-3216.
15. Day SE, Kettunen MI, Gallagher FA, et al. Detecting tumor response to treatment using hyperpolarized ^{13}C magnetic resonance imaging and spectroscopy. *Nat Med*. 2007;13(11):1382-1387.
16. Brindle KM, Campbell ID, Simpson RJ. A ^{1}H-NMR study of the activity expressed by lactate dehydrogenase in the human erythrocyte. *Eur J Biochem*. 1986;158(2):299-305.
17. Woessner DE. Nuclear transfer effects in nuclear magnetic resonance pulse experiments. *J Chem Phys*. 1961;35(1):41-48.
18. Hurd RE, Spielman D, Josan S, Yen Y-F, Pfefferbaum A, Mayer D. Exchange-linked dissolution agents in dissolution-DNP ^{13}C metabolic imaging. *Magn Reson Med*. 2013;70(4):936-942.
19. Hu S, Balakrishnan A, Bok RA, et al. ^{13}C-pyruvate imaging reveals alterations in glycolysis that precede c-*Myc*-induced tumor formation and regression. *Cell Metab*. 2011;14(1):131-142.
20. Johansson JE, Andren O, Andersson SO, et al. Natural history of early, localized prostate cancer. *JAMAJ Am Med Assoc*. 2004;291(22):2713-2719.
21. Trock BJ. Application of metabolomics to prostate cancer. *Urol Oncol*. 2011;29(5):572-581.
22. Jadvar H. Is there use for FDG-PET in prostate cancer? *Semin Nucl Med*. 2016;46(6):502-506.
23. Greenberg N, DeMayo F, Finegold M, et al. Prostate cancer in a transgenic mouse. *Proc Natl Acad Sci U S A*. 1995;92(8):3439-3443.
24. Albers MJ, Bok R, Chen AP, et al. Hyperpolarized ^{13}C lactate, pyruvate, and alanine: noninvasive biomarkers for prostate cancer detection and grading. *Cancer Res*. 2008;68(20):8607-8615.
25. Hill DK, Orton MR, Mariotti E, et al. Model free approach to kinetic analysis of real-time hyperpolarized ^{13}C magnetic resonance spectroscopy data. *PloS ONE*. 2013;8(9):e71996.
26. Zierhut ML, Yen YF, Chen AP, et al. Kinetic modeling of hyperpolarized $^{13}C_1$-pyruvate metabolism in normal rats and TRAMP mice. *J Magn Reson*. 2010;202(1):85-92.
27. Harris T, Eliyahu G, Frydman L, Degani H. Kinetics of hyperpolarized $^{13}C_1$-pyruvate transport and metabolism in living human breast cancer cells. *Proc Natl Acad Sci U S A*. 2009;106(43):18131-18136.
28. Sriram R, Van Criekinge M, Hansen A, et al. Real-time measurement of hyperpolarized lactate production and efflux as a biomarker of tumor aggressiveness in an MR compatible 3D cell culture bioreactor. *NMR Biomed*. 2015;28(9):1141-1149.
29. Nelson SJ, Kurhanewicz J, Vigneron DB, et al. Metabolic imaging of patients with prostate cancer using hyperpolarized [1-^{13}C] pyruvate. *Sci Transl Med*. 2013;5(198):198ra108.
30. Cunningham CH, Lau JY, Chen AP, et al. Hyperpolarized ^{13}C metabolic MRI of the human heart: initial experience. *Circ Res*. 2016;119(11):1177-1182.
31. Josan S, Hurd R, Park JM, et al. Dynamic metabolic imaging of hyperpolarized [2-^{13}C] pyruvate using spiral chemical shift imaging with alternating spectral band excitation. *Magn Reson Med*. 2014;71(6):2051-2058.
32. Schroeder MA, Lau AZ, Chen AP, et al. Hyperpolarized ^{13}C magnetic resonance reveals early-and late-onset changes to *in vivo* pyruvate metabolism in the failing heart. *Eur J Heart Fail*. 2013;15(2):130-140.
33. Schroeder MA, Atherton HJ, Ball DR, et al. Real-time assessment of Krebs cycle metabolism using hyperpolarized 13C magnetic resonance spectroscopy. *FASEB J*. 2009;23(8):2529-2538.
34. Hu S, Yoshihara HA, Bok R, et al. Use of hyperpolarized [1-^{13}C] pyruvate and [2-^{13}C] pyruvate to probe the effects of the anticancer agent dichloroacetate on mitochondrial metabolism in vivo in the normal rat. *Magn Reson Imaging*. 2012;30(10):1367-1372.
35. DeBerardinis RJ, Cheng T. Q's next: the diverse functions of glutamine in metabolism, cell biology and cancer. *Oncogene*. 2010;29(3):313-324.
36. Choi C, Ganji SK, DeBerardinis RJ, et al. 2-hydroxyglutarate detection by magnetic resonance spectroscopy in IDH-mutated patients with gliomas. *Nat Med*. 2012;18(4):624-629.
37. Mullard A. FDA approves first new sickle cell drug in 20 years. *Nat Rev Drug Discov*. 2017;16(8):519-519.
38. Keshari KR, Wilson DM. Chemistry and biochemistry of ^{13}C hyperpolarized magnetic resonance using dynamic nuclear polarization. *Chem Soc Rev*. 2014;43(5):1627-1659.

39. Salamanca-Cardona L, Shah H, Poot AJ, et al. *In vivo* imaging of glutamine metabolism to the oncometabolite 2-hydroxyglutarate in IDH1/2 mutant tumors. *Cell Metab*. 2017;26(6):830-841.
40. Gallagher FA, Kettunen MI, Day SE, Lerche M, Brindle KM. ^{13}C MR spectroscopy measurements of glutaminase activity in human hepatocellular carcinoma cells using hyperpolarized ^{13}C-labeled glutamine. *Magn Reson Med*. 2008;60(2):253-257.
41. Cabella C, Karlsson M, Canape C, et al. *In vivo* and *in vitro* liver cancer metabolism observed with hyperpolarized [5-^{13}C] glutamine. *J Magn Reson*. 2013;232:45-52.
42. Chaumeil MM, Larson PE, Yoshihara HA, et al. Non-invasive *in vivo* assessment of *IDH1* mutational status in glioma. *Nat Commun*. 2013;4:2429.
43. Gallagher FA, Kettunen MI, Hu D-E, et al. Production of hyperpolarized [1,4-$^{13}C_2$]malate from [1,4-$^{13}C_2$]fumarate is a marker of cell necrosis and treatment response in tumors. *Proc Natl Acad Sci U S A*. 2009;106(47):19801-19806.
44. Clatworthy MR, Kettunen MI, Hu D-E, et al. Magnetic resonance imaging with hyperpolarized [1,4-$^{13}C_2$] fumarate allows detection of early renal acute tubular necrosis. *Proc Natl Acad Sci U S A*. 2012;109(33):13374-13379.
45. Gatenby RA, Gillies RJ. Why do cancers have high aerobic glycolysis? *Nat Rev Cancer*. 2004;4(11):891-899.
46. Gallagher FA, Kettunen MI, Day SE, et al. Magnetic resonance imaging of pH in vivo using hyperpolarized 13C-labelled bicarbonate. *Nature*. 2008;453:940.
47. Flavell RR, von Morze C, Blecha JE, et al. Application of Good's buffers to pH imaging using hyperpolarized ^{13}C MRI. *Chem Commun*. 2015;51(74):14119-14122.
48. Düwel S, Hundshammer C, Gersch M, et al. Imaging of pH in vivo using hyperpolarized 13C-labelled zymonic acid. *Nat Commun*. 2017;8:15126.
49. Jiang W, Lumata L, Chen W, et al. Hyperpolarized 15N-pyridine derivatives as pH-sensitive MRI agents. *Sci Rep*. 2015;5:9104.
50. Pruessmann KP, Weiger M, Scheidegger MB, Boesiger P. SENSE: sensitivity encoding for fast MRI. *Magn Reson Med*. 1999;42(5):952-962.
51. Roemer PB, Edelstein WA, Hayes CE, Souza SP, Mueller OM. The NMR phased array. *Magn Reson Med*. 1990;16(2):192-225.
52. Sodickson DK, Griswold MA, Jakob PM. SMASH imaging. *Magn Reson Imaging Clin N Am*. 1999;7(2):237-254. vii-viii
53. Edelstein WA, Glover GH, Hardy CJ, Redington RW. The intrinsic signal-to-noise ratio in NMR imaging. *Magn Reson Med*. 1986;3(4):604-618.
54. Dominguez-Viqueira W, Lau AZ, Chen AP, Cunningham CH. Multichannel receiver coils for improved coverage in cardiac metabolic imaging using prepolarized ^{13}C substrates. *Magn Reson Med*. 2012;70(1):295-300.
55. Arunachalam A, Whitt D, Fish K, et al. Accelerated spectroscopic imaging of hyperpolarized C-13 pyruvate using SENSE parallel imaging. *NMR Biomed*. 2009;22(8):867-873.
56. Feng Y, Gordon JW, Shin PJ, et al. Development and testing of hyperpolarized ^{13}C MR calibrationless parallel imaging. *J Magn Reson*. 2016;262:1-7.
57. Ohliger MA, Larson PE, Bok RA, et al. Combined parallel and partial Fourier MR reconstruction for accelerated 8-channel hyperpolarized carbon-13 in vivo magnetic resonance spectroscopic imaging (MRSI). *J Magn Reson Imaging*. 2013;38(3):701-713.
58. Tropp J, Lupo JM, Chen A, et al. Multi-channel metabolic imaging, with SENSE reconstruction, of hyperpolarized [1-^{13}C] pyruvate in a live rat at 3.0 tesla on a clinical MR scanner. *J Magn Reson*. 2011;208(1):171-177.
59. Mayer D, Yen YF, Takahashi A, et al. Dynamic and high-resolution metabolic imaging of hyperpolarized [1-^{13}C]-pyruvate in the rat brain using a high-performance gradient insert. *Magn Reson Med*. 2010;65(5):1228-1233.
60. Chen AP, Tropp J, Hurd RE, et al. *In vivo* hyperpolarized ^{13}C MR spectroscopic imaging with ^{1}H decoupling. *J Magn Reson*. 2009;197(1):100-106.
61. Marjanska M, Iltis I, Shestov AA, et al. *In vivo* ^{13}C spectroscopy in the rat brain using hyperpolarized [1-^{13}C]pyruvate and [2-^{13}C]pyruvate. *J Magn Reson*. 2010;206(2):210-218.
62. Mishkovsky M, Cheng T, Comment A, Gruetter R. Localized in vivo hyperpolarization transfer sequences. *Magn Reson Med*. 2012;68(2):349-352.
63. Wang J, Kreis F, Wright AJ, Hesketh RL, Levitt MH, Brindle KM. Dynamic ^{1}H imaging of hyperpolarized [1-^{13}C]lactate in vivo using a reverse INEPT experiment. *Magn Reson Med*. 2017. https://doi.org/10.1002/mrm.26725
64. Morris GA, Freeman R. Enhancement of nuclear magnetic-resonance signals by polarization transfer. *J Am Chem Soc*. 1979;101(3):760-762.
65. Kohler SJ, Yen Y, Wolber J, et al. In vivo ^{13}carbon metabolic imaging at 3T with hyperpolarized ^{13}C-1-pyruvate. *Magn Reson Med*. 2007;58(1):65-69.
66. Zhao L, Mulkern R, Tseng CH, et al. Gradient-echo imaging considerations for hyperpolarized ^{129}Xe MR. *J Magn Reson B*. 1996;113(2):179-183.
67. Cunningham CH, Chen AP, Albers MJ, et al. Double spin-echo sequence for rapid spectroscopic imaging of hyperpolarized ^{13}C. *J Magn Reson*. 2007;187(2):357-362.
68. Chen AP, Albers MJ, Cunningham CH, et al. Hyperpolarized C-13 spectroscopic imaging of the TRAMP mouse at 3T—initial experience. *Magn Reson Med*. 2007;58(6):1099-1106.
69. Larson PE, Bok R, Kerr AB, et al. Investigation of tumor hyperpolarized [1-^{13}C]-pyruvate dynamics using time-resolved multiband RF excitation echo-planar MRSI. *Magn Reson Med*. 2010;63(3):582-591.
70. Noll DC, Nishimura DG, Macovski A. Homodyne detection in magnetic resonance imaging. *IEEE Trans Med Imaging*. 1991;10(2):154-163.
71. Hu S, Lustig M, Chen AP, et al. Compressed sensing for resolution enhancement of hyperpolarized 13C flyback 3D-MRSI. *J Magn Reson*. 2008;192(2):258-264.
72. Lustig M, Donoho DL, Santos JM, Pauly JM. Compressed sensing MRI. *IEEE Signal Process Mag*. 2008;25(2):72-82.
73. Hu S, Lustig M, Balakrishnan A, et al. 3D compressed sensing for highly accelerated hyperpolarized ^{13}C MRSI with in vivo applications to transgenic mouse models of cancer. *Magn Reson Med*. 2010;63(2):312-321.
74. Larson PE, Hu S, Lustig M, et al. Fast dynamic 3D MR spectroscopic imaging with compressed sensing and multiband excitation pulses for hyperpolarized 13C studies. *Magn Reson Med*. 2011;65(3):610-619.
75. Levin YS, Mayer D, Yen YF, Hurd RE, Spielman DM. Optimization of fast spiral chemical shift imaging using least squares reconstruction: application for hyperpolarized ^{13}C metabolic imaging. *Magn Reson Med*. 2007;58(2):245-252.
76. Mayer D, Yen YF, Tropp J, Pfefferbaum A, Hurd RE, Spielman DM. Application of subsecond spiral chemical shift imaging to real-time multislice metabolic imaging of the rat in vivo after injection of hyperpolarized $^{13}C_1$-pyruvate. *Magn Reson Med*. 2009;62(3):557-564.

77. Larson PE, Kerr AB, Chen AP, et al. Multiband excitation pulses for hyperpolarized ^{13}C dynamic chemical-shift imaging. *J Magn Reson*. 2008;194(1):121-127.

78. Leupold J, Mansson S, Petersson JS, Hennig J, Wieben O. Fast multiecho balanced SSFP metabolite mapping of ^{1}H and hyperpolarized ^{13}C compounds. *Magn Reson Mater Phys Biol Med*. 2009;22(4):251-256.

79. Wiesinger F, Weidl E, Menzel MI, et al. IDEAL spiral CSI for dynamic metabolic MR imaging of hyperpolarized [1-^{13} C]pyruvate. *Magn Reson Med*. 2011;68(1):8-16.

80. Gordon JW, Vigneron DB, Larson PE. Development of a symmetric echo planar imaging framework for clinical translation of rapid dynamic hyperpolarized 13 C imaging. *Magn Reson Med*. 2017;77(2):826-832.

81. Lau AZ, Chen AP, Hurd RE, Cunningham CH. Spectral-spatial excitation for rapid imaging of DNP compounds. *NMR Biomed*. 2011;24(8):988-996.

82. Miller JJ, Lau AZ, Teh I, et al. Robust and high resolution hyperpolarized metabolic imaging of the rat heart at 7 T with 3D spectral-spatial EPI. *Magn Reson Med*. 2016;75(4):1515-1524.

83. Meyer CH, Pauly JM, Macovski A, Nishimura DG. Simultaneous spatial and spectral selective excitation. *Magn Reson Med*. 1990;15(2):287-304.

84. Schick F, Forster J, Machann J, Kuntz R, Claussen CD. Improved clinical echo-planar MRI using spatial-spectral excitation. *J Magn Reson Imaging*. 1998;8(4):960-967.

85. Cunningham CH, Chen AP, Lustig M, et al. Pulse sequence for dynamic volumetric imaging of hyperpolarized metabolic products. *J Magn Reson*. 2008;193(1):139-146.

86. Gordon JW, Milshteyn E, Marco-Rius I, Ohliger M, Vigneron DB, Larson PEZ. Mis-estimation and bias of hyperpolarized apparent diffusion coefficient measurements due to slice profile effects. *Magn Reson Med*. 2017;78(3):1087-1092.

87. Shin PJ, Larson PE, Ohliger MA, et al. Calibrationless parallel imaging reconstruction based on structured low-rank matrix completion. *Magn Reson Med*. 2014;72(4):959-970.

88. Dominguez-Viqueira W, Geraghty BJ, Lau JY, Robb FJ, Chen AP, Cunningham CH. Intensity correction for multichannel hyperpolarized ^{13}C imaging of the heart. *Magn Reson Med*. 2016;75(2):859-865.

89. Yen YF, Le Roux P, Mayer D, et al. T_2 relaxation times of ^{13}C metabolites in a rat hepatocellular carcinoma model measured in vivo using ^{13}C-MRS of hyperpolarized [1-^{13}C]pyruvate. *NMR Biomed*. 2010;23(4):414-423.

90. Johansson E, Månsson S, Wirestam R, et al. Cerebral perfusion assessment by bolus tracking using hyperpolarized ^{13}C. *Magn Reson Med*. 2004;51(3):464-472.

91. Svensson J, Månsson S, Johansson E, Petersson JS, Olsson LE. Hyperpolarized ^{13}C MR angiography using trueFISP. *Magn Reson Med*. 2003;50(2):256-262.

92. von Morze C, Larson PE, Hu S, et al. Imaging of blood flow using hyperpolarized [^{13}C]urea in preclinical cancer models. *J Magn Reson Imaging*. 2011;33(3):692-697.

93. Reed GD, von Morze C, Bok R, et al. High resolution ^{13}C MRI with hyperpolarized urea: in vivo T_2 mapping and ^{15}N labeling effects. *IEEE Trans Med Imaging*. 2014;33(2):362-371.

94. Reed GD, von Morze C, Verkman AS, et al. Imaging renal urea handling in rats at millimeter resolution using hyperpolarized magnetic resonance relaxometry. *Tomography*. 2016;2(2):125-135.

95. Mansson S, Petersson JS, Scheffler K. Fast metabolite mapping in the pig heart after injection of hyperpolarized ^{13}C-pyruvate with low-flip angle balanced steady-state free precession imaging. *Magn Reson Med*. 2012;68(6):1894-1899.

96. von Morze C, Sukumar S, Reed GD, et al. Frequency-specific SSFP for hyperpolarized ^{13}C metabolic imaging at 14.1 T. *Magn Reson Imaging*. 2013;31(2):163-170.

97. Shang H, Sukumar S, von Morze C, et al. Spectrally selective three-dimensional dynamic balanced steady-state free precession for hyperpolarized C-13 metabolic imaging with spectrally selective radiofrequency pulses. *Magn Reson Med*. 2017;78(3):963-975.

How to cite this article: von Morze C, Merritt ME. Cancer in the crosshairs: targeting cancer metabolism with hyperpolarized carbon-13 MRI technology. *NMR in Biomedicine*. 2019;32:e3937. https://doi.org/10.1002/nbm.3937